Selective reduction of CO_2 to CO under visible light by controlling coordination structures of CeO_x-S/$ZnIn_2S_4$ hybrid catalysts

Tingting Hou[a,b], Nengchao Luo[a,b], Yi-Tao Cui[c], Jianmin Lu[a], Lei Li[d], Katherine E. MacArthur[e], Marc Heggen[e], Ruotian Chen[a,b], Fengtao Fan[a], Wenming Tian[f], Shengye Jin[f], Feng Wang[a,*]

[a] State Key Laboratory of Catalysis, Dalian National Laboratory for Clean Energy, Dalian Institute of Chemical Physics, Chinese Academy of Sciences, Dalian, 116023, PR China
[b] University of Chinese Academy of Sciences, Beijing, 100049, PR China
[c] Synchrotron Radiation Laboratory, Laser and Synchrotron Research Center (LASOR), The Institute for Solid State Physics, The University of Tokyo, 1-490-2 Kouto, Shingu-cho Tatsuno, Hyogo, 679-5165, Japan
[d] Synchrotron Radiation Nanotechnology Center, University of Hyogo, 1-490-2 Kouto, Shingu-cho Tatsuno, Hyogo, 679-5165, Japan
[e] Ernst Ruska Centre for Microscopy and Spectroscopy with Electrons and Peter Grünberg Institute, Forschungszentrum Juelich GmbH, Juelich, 52425, Germany
[f] State Key Laboratory of Molecular Reaction Dynamics and Collaborative Innovation Center of Chemistry for Energy Materials (iChEM), Dalian Institute of Chemical Physics, Chinese Academy of Sciences, Dalian, 116023, PR China

ARTICLE INFO

ABSTRACT

Engineering the electronic properties of heterogeneous catalysts is an important strategy to enhance their activity towards CO_2 reduction. Herein, we prepared partially sulfurized cerium oxide (CeO_x-S) nanoclusters with the size less than 2 nm on the surface of $ZnIn_2S_4$ layers. Surface electronic properties of CeO_x-S nanoclusters are facilely modulated by cerium coordination to sulfur, inducing the emergence of abundant Ce^{3+} and oxygen vacancies. For the photoreduction of CO_2, CeO_x-S/$ZnIn_2S_4$ hybrid catalysts exhibited a CO productivity of 1.8 mmol g^{-1} with a rate of 0.18 mmol $g^{-1} h^{-1}$, which was twice as higher as that of $ZnIn_2S_4$ catalyst using triethylamine as a sacrificial electron donor. Further mechanistic studies reveal that the photogenerated electrons are trapped by oxygen vacancies on CeO_x-S/$ZnIn_2S_4$ catalysts and subsequently transfer to CO_2, benefiting the activation of CO_2. Moreover, the extremely high selectivity of CO is derived from the weak adsorption of CO on the surface of CeO_x-S/$ZnIn_2S_4$ catalysts.

1. Introduction

Due to superfluous consumption of fossil fuels, anthropogenic emissions of CO_2 to the atmosphere are rapidly increasing, which gives rise to the global warming [1–8]. In this case, reduction of CO_2 into valuable carbon forms has attracted intensive attention around the world [9–12]. Despite of the promising future, this approach faces a grand challenge because of the extremely high stability of CO_2 molecule [3]. Both experimental and theoretical results show that electron transfer to CO_2 initiates the reduction steps [13–15]. Therefore, the activation of CO_2 is significantly influenced by the surface electronic properties of catalysts. Thanks to the efforts from several groups, catalyst surfaces endowed with high density of negative charges are found to be active in CO_2 chemical transformation [2,10].

Loading noble metals to semiconductors is an efficient strategy to accumulate electrons on the surface of catalysts, thereby improving the catalytic performance in the photocatalytic CO_2 reduction [16]. Metal

oxide photocatalysts show low activity due to weak adsorption and activation of CO_2 [17]. Creating defective sites, such as oxygen vacancies, on the surface of oxides is considered as another effective strategy to increasing the surface negative charge density. Positive electrostatic field on the oxygen vacancies can accumulate extra negative charges during photo irradiation, endowing the metal oxides with the potential to activate CO_2 [18,19]. Several common methods are usually adopted to create defects: (1) pretreatment of the as-prepared oxides under inert or reductive atmosphere [20,21]; (2) controlling the size or morphology of oxides [22,23]; (3) hybridizing oxides with chalcogenide. For example, oxygen-deficient mesoporous WO_3 prepared by H_2 treatment showed high activity of photocatalytic CO_2 reduction, which was about 22 times that of perfect mesoporous WO_3 [20]. Sun et al synthesized the ultrathin $WO_3 \cdot 0.33H_2O$ nanotubes with a large amount of exposed surface defective sites, realizing excellent catalytic performance in CO_2 photoreduction [22]. Very recently, Yang et al. [24] and Wang et al. [8] adopted $ZnIn_2S_4$ to couple with CeO_2 and

In_2O_3, respectively, and the yield $CeO_2/ZnIn_2S_4$ microspheres and $ZnIn_2S_4$-In_2O_3 hierarchical tubular nanostructures exhibited remarkably enhanced photocatalytic activity during CO_2 reduction. Given the superiority of the defects in facilitating CO_2 reduction, exploiting new methodologies to design and synthesize highly efficient photocatalysts is of great importance and high demand for CO_2 reduction.

Herein, we developed a "partial sulfurization" strategy to construct surface defective sites of CeO_x nanoclusters, which can greatly enhance the activity of photocatalytic CO_2 reduction. We initially constructed the CeO_x-S/$ZnIn_2S_4$ hybrid catalyst via a one-pot hydrothermal method. High-angle annular dark-field scanning transmission electron microscopy (HAADF-STEM) directly reflects the high dispersion of CeO_x-S with size of less than 2 nm. Extended X-ray absorption fine structure (EXAFS) confirms the structure of partially sulfurized cerium oxide nanoclusters. The partial sulfurization results in plentiful Ce^{3+} and oxygen vacancies, confirmed by X-ray absorption near edge structure (XANES), X-ray photoelectron spectroscopy (XPS) and electron paramagnetic resonance (EPR) characterizations. For the photoreduction of CO_2, CeO_x-S/$ZnIn_2S_4$ hybrid catalyst behaved the enhanced catalytic activity with a CO production rate of 0.18 mmol g^{-1} h^{-1} under visible light, which is two times of that for the pristine $ZnIn_2S_4$. Further mechanistic studies unveil that the oxygen vacancies in CeO_x-S/$ZnIn_2S_4$ hybrid catalyst trap the photogenerated electrons to activate and reduce CO_2. Moreover, this defective structure endows unique surface electronic properties of the catalyst, thereby increasing adsorption energy of CO_2 and lowering its activation energy barrier. Meanwhile, due to the weak adsorption of CO, noble metal-free CeO_x-S/$ZnIn_2S_4$ catalyst affords an excellent selectivity (> 99%) of CO for CO_2 photoreduction.

2. Experimental section

2.1. Materials

$ZnSO_4·7H_2O$ (99.5%), $InCl_3·4H_2O$ (99.9%), $CeCl_3·7H_2O$ (99.9%), polyethylene glycol 6000 (PEG-6000) and thioacetamide (TAA, 99%) were purchased from Shanghai Aladdin Bio-Chem Technology Co., Ltd. Ethylene glycol (AR) was purchased from Sinopharm Chemical Reagent Co., Ltd. All reagents were used without further purification.

2.2. Preparation of $ZnIn_2S_4$ catalysts

$ZnIn_2S_4$ was prepared according to the literature [25]. Typically, 294.0 mg of $ZnSO_4·6H_2O$ (294.0 mg), 624.2 mg of $InCl_3·4H_2O$, and 260.6 mg of PEG-6000 were dissolved in 20 mL of ethylene glycol in a 50-mL Teflon vessel, followed by magnetically stirring for 30 min at room temperature. 604.8 mg of TAA was then added into the above solution and stirred for another 30 min. Finally, the mixture was tightly sealed and placed in a 160 °C oven. After aging for 20 h, the autoclave was then naturally cooled to room temperature and washed with absolute ethanol (3 × 40 mL) and deionized water (2 × 40 mL). A yellow solid was finally obtained after being dried in vacuum at 60 °C for 12 h.

2.3. Preparation of CeO_x-S/$ZnIn_2S_4$ catalysts

Ultra-fine CeO_x-S nanoclusters highly dispersed on $ZnIn_2S_4$ were prepared by a facile one-pot hydrothermal method. Typically, 294.0 mg of $ZnSO_4·6H_2O$ (294.0 mg), 624.2 mg of $InCl_3·4H_2O$, 105.0 mg of $CeCl_3·7H_2O$ and 260.6 mg of PEG-6000 were dissolved in 20 mL of ethylene glycol in a 50-mL Teflon vessel, followed by magnetically stirring for 30 min at room temperature. 604.8 mg of TAA was then added into the above solution and stirred for another 30 min. Finally, the mixture was tightly sealed and placed in a 160 °C oven. After aging for 20 h, the autoclave was then naturally cooled to room temperature and washed with absolute ethanol (3 × 40 mL) and deionized water (2 × 40 mL). A yellow solid was finally obtained after being dried in vacuum at 60 °C for 12 h. The Ce content was determined as 1.55 wt% by inductively coupled plasma optical emission spectrometer (ICP-OES).

2.4. Photocatalytic CO_2 reduction

Photocatalytic reactions were conducted in a home-made LED photoreactor (Figure S1). The cylinder in gray is the supporting system for LED array. The blue semispheres represent the LED lamps which spread on the supporting system with a 6 × 2 mode. The light green tube represents the quartz tube for reaction, but the actual color of the quartz tube is colorless and transparent. The external diameter, wall thickness and volume of the quartz tube is 13 mm, 1.5 mm and 6.98 mL, respectively.

Photocatalytic reactions were conducted in a home-made quartz photoreactor with a total power of 9.0 W (455 nm LEDs). In a typical photocatalytic CO_2 reduction reaction, 10 mg of photocatalysts, 0.5 mL of H_2O, 0.5 mL of acetonitrile (MeCN) and 0.1 mL of triethylamine were added into a 6-mL photoreactor. The 9 W LEDs centred at 455 nm were used as light source. Before irradiation, high purity CO_2 gas (99.99%) was introduced into the reactor for 3 min. During the photocatalytic process, the temperature of the reaction system was kept below 42 °C and the reaction system was vigorously stirred with a magnetic stirrer. After the reaction, the gas sample was qualitatively analyzed by a Techcomp GC 7900 gas chromatograph (TCD detector, TDX-01 column) by identifying the chromatographic peaks with pure He as the internal standard. *CAUTION: Specific protection by wearing eye goggles to shield 455 nm light is mandatory to avoid injuring eyes.*

2.5. Measurement of AQY

The AQY measurement for CO formation was carried out in a quartz topirradiation-type reaction vessel with a power of 30 W (455 nm LED light, FWHM = 20 nm). The number of photons reaching the reaction solution was measured using a calibrated Si photodiode (LS-100, EKO Instruments Co., Ltd.). The AQY was calculated according to the following equation: $AQY(\%) = [2 × (R_1 + R_2)/I] × 100$. In this equation, R_1, R_2 and I represent the rates of CO production, H_2 production and incident photons, respectively. It was assumed that all incident photons were absorbed by the suspension. The total number of incident photons at the wavelength of 455 nm was measured to be $5.99 × 10^{21}$ photons per h.

2.6. General characterizations

Powder X-ray diffraction patterns (XRD) were conducted with a PANalytical X-Pert PRO diffractometer, using Cu-Kα radiation at 40 kV and 20 mA. Continuous scans were collected in the 2θ range of 10-80°. Morphologies of the as-prepared $ZnIn_2S_4$ and CeO_x-S/$ZnIn_2S_4$ were observed by transmission electron microscopy (TEM, JEOL JEM-2100).

Scanning transmission electron microscopy (STEM) was performed using an FEI Titan 80–200 (ChemiSTEM) electron microscope operated at 200 kV, equipped with a spherical aberration (Cs) probe corrector (CEOS GmbH) and a high-angle annular dark-field (HAADF) detector. A probe semi-angle of 25.1 mrad and an inner collection semi-angle of the detector of 67.9 mrad were used. Compositional maps were obtained with energy-dispersive X-ray spectroscopy (EDX) using the Super-X quadrant system which has four silicon drift detectors aligned symmetrically around the pole piece resulting in a combined solid angle of 0.7 srad. For EDX analysis, Zn K, In K, S K, O K and Ce L peaks were used. High-resolution transmission electron microscopy (HRTEM) investigations were performed using an FEI-Titan 80–300 electron microscope equipped with a Cs corrector for the objective lens. The microscope was operated at a voltage of 300 kV using the negative-Cs imaging technique (NCSI, with Cs set at around ~13 μm and defocus around +6 nm).

The X-ray absorption fine structure (XAFS) experiment was

performed at the bending magnet beamline BL08B2 of SPring-8 (8 GeV, 100 mA) belong to Hyogo-prefectural, in which, the X-ray beam was monochromatized with water-cooled Si (111) double-crystal monochromator and focused with two Rh coated focusing mirrors with the beam size of 2.0 mm in the horizontal direction and 0.5 mm in the vertical direction around sample position [26]. The samples were filled in a phi10 stainless tube for XAFS measurements. All of the samples were measured by both transmission and fluorescence modes at both Ce L₃- and K-edge. The spectra were analyzed and fitted using an analysis program Demeter [27]. The wavelet simulation was carried out with continuous Cauchy wavelet transform method [28]. For EXAFS fittings, the crystal structures of CeO_2 and Ce_2S_3 are from Materials Project (https://materialsproject.org). For CeO_x-S/$ZnIn_2S_4$ sample, the structure from DFT calculation is used.

X-ray photoelectron spectroscopy (XPS) analyses were performed at ESCALAB250Xi (Thermo, USA) using Al-Kα (1486.6 eV) as the exciting source. Basic pressure of the system was 3×10^{-8} Pa.

Kelvin probe force microscopy (KPFM). The FTO glasses (resistivity, 0.01 Ω•cm) were cleaned according to the literature [29]. Firstly, the original FTO glasses were cleaned with acetone (30 min), ethanol (30 min) and H_2O (30 min) by ultrasonic. Then a suspension of $ZnIn_2S_4$ or CeO_x-S/$ZnIn_2S_4$ in ethanol that was obtained by ultrasonication for 5 h was added dropwise (5 drops, another drop of the suspension was added after the ethanol of the previous one dried up). Prior to Kelvin probe force microscopy (KPFM) measurements, the FTO glasses were treated in vacuum at 150 °C for 2 h. The CPD signals were measured by AM-KPFM on a Bruker Dimension V SPM system equipped with Pt/Ir coated tips (resonant frequency 72 kHz). 400-nm light with light intensity of 2 mW·cm⁻² was used to excite the samples. The contact potential difference is defined as the difference between work functions of the tip and the sample. The CPD values of all samples were calibrated with one same tip.

Time-resolved fluorescence measurements were performed using a photoluminescence (PL)-scanned imaging microscope coupled with a time-correlated single photon counting (TCSPC) module. The excitation wavelength was 406 nm, and the PL signal was collected using a high-speed detector (HPM-100-50, Hamamatsu, Japan) with a 420 nm long pass filter and 595 ± 30 nm band pass filter.

Electron paramagnetic resonance (EPR) spectra were taken on a Bruker spectrometer in the X-band at 77 K with a field modulation of 100 kHz. The microwave frequency was maintained at 9.4 GHz. Firstly, 10 mg of catalyst was put into a home-made paramagnetic tube. After vacuuming the reaction tube, the spectrum in dark was recorded. Then the semiconductor laser centered at 440 nm (200 mW·cm⁻²) was switched on. After irradiating for 5 min, the spectrum in light was recorded. Then after turning off the photosource and recording the spectrum again, pure CO_2 was injected into the tube at room temperature and then the spectrum was recorded at 77 K.

In situ FTIR spectra were collected in Bruker 70 IR spectrometer at a resolution of 4 cm⁻¹. Before CO_2 and H_2O adsorption, the samples were treated in a FTIR cell with pure Ar at 150 °C for 0.5 h, then cooled to room temperature. After pretreatment, a background spectrum was recorded for each sample using 16 scans and was then subtracted automatically from the subsequent spectra. Each sample was then exposed to a flowing water vapor of CO_2/Ar and adsorption spectra were recorded after adsorption 20 min in dark. Then the semiconductor laser centered at 440 nm (200 mW·cm⁻²) was switched on and IR spectrum was recorded at intervals.

2.7. DFT calculations

We have employed the Vienna Ab Initio Package (VASP) [30,31] to carry out all the density functional theory (DFT) calculations within the generalized gradient approximation (GGA) using the PBE [32] function. We have chosen the projected augmented wave (PAW) pseudopotentials [33,34] to describe the ionic cores and take valence electrons into

account using a plane wave basis set with an energy cutoff of 400 eV. Partial occupancies of the Kohn − Sham orbitals were allowed using the Gaussian smearing method and a width of 0.10 eV. The electronic energy was considered self-consistent when the energy change was smaller than 10^{-5} eV. Gamma-point of Brillouin zone was used for k-point sampling. A geometry optimization was considered convergent when the energy change was smaller than 10^{-4} eV. Grimme's DFT-D3 methodology [35] was used to describe the dispersion interactions among all the atoms. DFT + U was chosen for the Ce 4f electrons with U = 5.0 eV to mitigate the self-interaction error (SIE).

The gas phase molecules of CO_2 and CO, and the free-standing Ce_6O_{10} and $Ce_6O_9S_1$ clusters were put in a cubic box with a side length of 20 Angstroms. The surfaces of $ZnIn_2S_4$ (0001) supporting Ce_6O_{10} and $Ce_6O_9S_1$ clusters are slab surfaces. The equilibrium lattice constants of bulk $ZnIn_2S_4$ hexagonal unit cell were calculated, when using an $11 \times 11 \times 2$ Monkhorst-Pack grid for Brillouin zone sampling, to be a = b = 3.896 Å and c = 24.498 Å, which agree well with experimental ones [36]. This unit cell was used to construct the $ZnIn_2S_4$ (0001) surface with a $p(4 \times 4)$ periodicity and 7 atomic layers (S-Zn-S-In-S-In-S) with a 15 Å of vacuum in the c/z direction between the surface and its periodic images. During geometry optimization, the middle S-In-S layers were fixed to their bulk configuration while the rest 4 layers were allowed to fully relax.

3. Results and discussion

3.1. Structural characterization of the photocatalysts

CeO_x-S/$ZnIn_2S_4$ hybrid catalyst was prepared by a facile one-pot hydrothermal method. All the X-ray diffraction (XRD) peaks exclusively show typical diffraction patterns of hexagonal $ZnIn_2S_4$ without any characteristic peaks of cerium compounds including CeO_2, Ce_2O_3 or Ce_2S_3, indicating the ultra-fine dispersion of Ce species (Figure S2) [25,37,38]. The as-prepared CeO_x-S/$ZnIn_2S_4$ hybrid catalyst presents as nanoflowers with lamellar structure (Fig. 1 and Figure S3). The lattice fringes of 3.28 Å and 4.17 Å are attributed to the (102) and (006) interplanar distance of $ZnIn_2S_4$ [39]. HAADF-STEM and energy dispersive X-ray (EDX) mapping were used to further characterize the morphology and distribution of Ce species. Whilst the EDX map in Fig. 1 is very noisy, the presence of Ce was confirmed by a low magnification sum spectrum where the signal of Ce element is well above the background signal (Figure S4). Sub-nanometer EDX mapping shows a uniform dispersion of Ce, Zn, In and S elements (Fig. 1b-f). Specially, Ce species are finely dispersed on the surface of $ZnIn_2S_4$ layers as nanoclusters with the size of less than 2 nm, highlighted by yellow circles in Fig. 1b.

To further confirm the coordination structure of the CeO_x-S/$ZnIn_2S_4$ hybrid catalyst, we performed the XAFS characterizations (Fig. 2, Table 1 and Figures S4-S6). In order to avoid the fluorescence peak background from other elements, and give clear Ce structure information, the Ce K edge EXAFS was measured for structure analysis. The EXAFS of CeO_x-S/$ZnIn_2S_4$ was plotted with standard samples as shown in Fig. 2a. The Ce–O and Ce–S have different distances in standard samples, making it possible to distinguish them clearly in CeO_x-S/ $ZnIn_2S_4$. The EXAFS fitting results for CeO_x-S/$ZnIn_2S_4$ in R- and k- space are represented in Figs. 2b and c (Figure S7 for standard samples) with the parameters in Table 1. The Ce element in CeO_x-S/$ZnIn_2S_4$ hybrid catalyst is mainly coordinated with oxygen. The coordination number of Ce derived from Ce–O coordination is 1.98 ± 0.32, indicative of coordinative unsaturated Ce species, which resembles that of CeO_x. Besides, the small amount of Ce–S can also be observed and the coordination number of Ce derived from Ce–S is 0.39 ± 0.35, indicating the partially sulfurized cerium oxide nanoclusters. Both the EXAFS fitting results (Fig. 2a) and the wavelet analysis (Figure S5) suggest that in high R or k region, the high order or long-distance scattering is too weak to be distinguished from noises, suggesting a fine-dispersion structure of Ce. The results highly correspond to our HAADF-STEM and
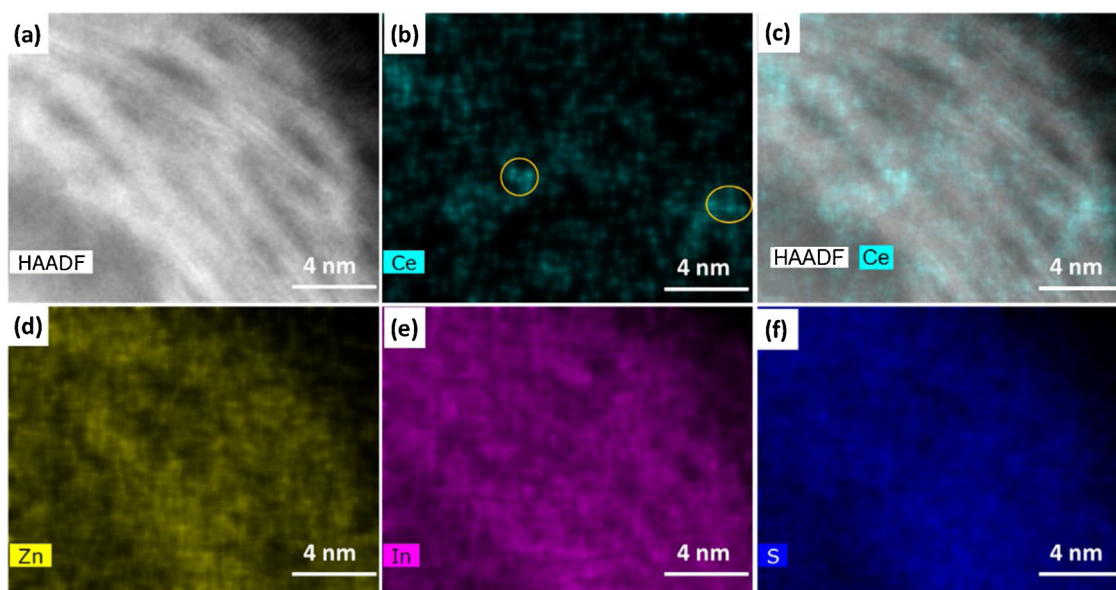
Fig. 1. HAADF-STEM and EDX mapping images of CeO_x-$S/ZnIn_2S_4$. (a) HAADF-STEM image. (b) EDX mapping of Ce element. (c) Overlapping HAADF-STEM images with Ce element EDX mapping. (d) EDX mapping of Zn element. (e) EDX mapping of In element. (f) EDX mapping of S element.
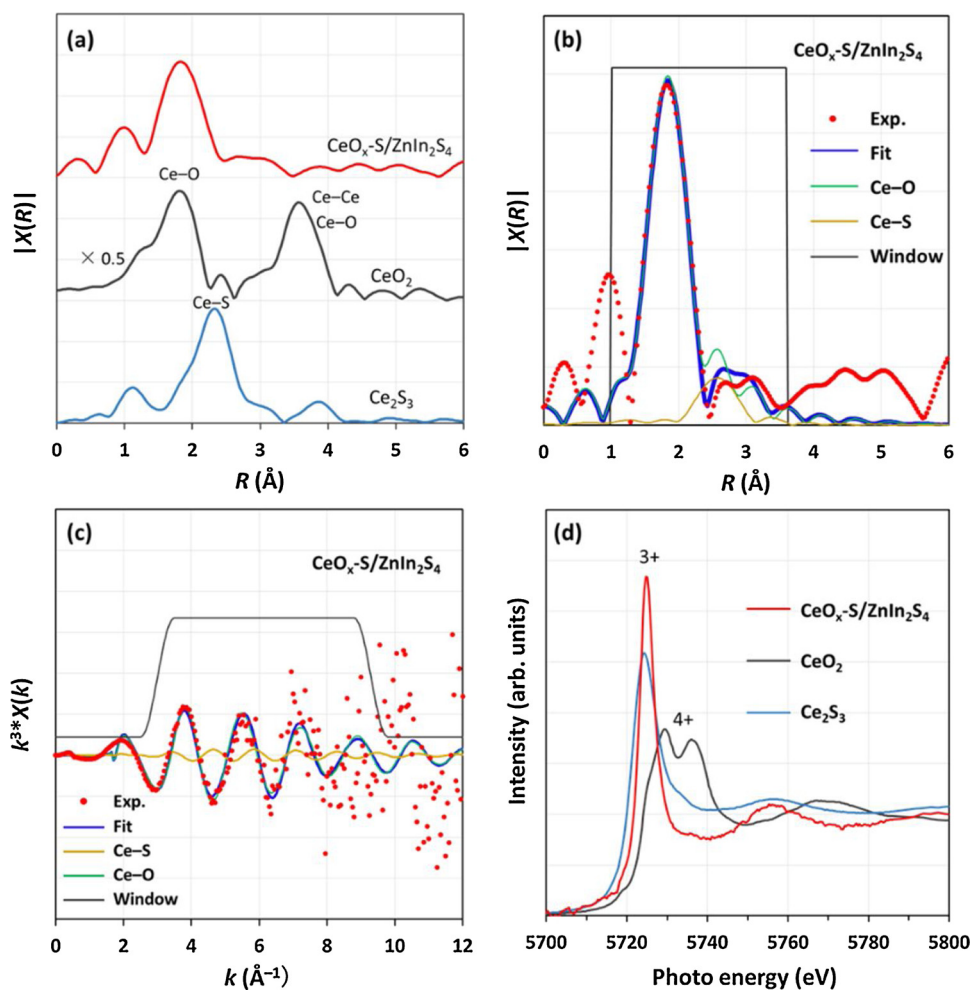

Fig. 2. The XAFS spectra of CeO_x-$S/ZnIn_2S_4$ hybrid catalyst together with CeO_2, Ce_2S_3 standard samples. (a) Ce K edge EXAFS spectra for CeO_x-$S/ZnIn_2S_4$ hybrid catalyst, CeO_2 and Ce_2S_3. The fitting results in both (b) R- and (c) k- space for CeO_x-$S/ZnIn_2S_4$ with k^3 powered. (d) Ce L3 edge XANES spectra for CeO_x-$S/ZnIn_2S_4$ hybrid catalyst, CeO_2 and Ce_2S_3.

Table 1
The fitting parameters of CeO_x-S/$ZnIn_2S_4$, CeO_2 and Ce_2S_3.[a]

Sample	Shell	CN	R(Å)	ΔE_0 (eV)	$\Delta \delta^2$ (Å^2)
CeO_x-S/$ZnIn_2S_4$	Ce–O	1.98	2.24	10.6	0.0067
	Ce–S	0.39	2.97	10.6	0.0094
CeO_2	Ce–O	8	2.36	5.4	0.0053
	Ce–Ce	12	3.83	5.4	0.0053
Ce_2S_3	Ce–S	5	2.94	0.26	0.0101

[a] The R, CN, ΔE_0, and $\Delta \delta^2$ denote interatomic distance, coordination number, the inner potential correction and Debye-Waller factor, respectively. The data ranges used for data fitting are 3.0-12 Å^{-1} in k-space, 1.0–4.5 Å in R-space for CeO_2, 3.0-12 Å^{-1} in k-space, 1.3–3 Å in R-space for Ce_2S_3 and 3.0-9.5 Å^{-1} in k-space, 1.0–3.4 Å in R-space for CeO_x-S/$ZnIn_2S_4$, respectively.

EDX results (Figs. 1b, c). The Ce L3 edge XANES spectra for different samples were presented in Fig. 2d. The CeO_2 spectrum shows the clear tetra-valence features as reported in former work [40–43], while the Ce species in CeO_x-S/$ZnIn_2S_4$ and Ce_2S_3 show tri-valence features. In addition, both the white line shape and the energy shift of CeO_x-S/$ZnIn_2S_4$ hybrid catalyst are the same as reported ones of $Ce(NO_3)_3$ and Ce_2O_3 [40–43]. It suggests that Ce in CeO_x-S/$ZnIn_2S_4$ hybrid catalyst possesses a nearly tri-valence state. XPS experiment was conducted to further investigate the surface oxidation state of Ce element in CeO_x-S/$ZnIn_2S_4$ hybrid catalyst (Fig. 3a). According to the previous work [44], the peaks marked as u (900.8 eV) and u''' (923.2 eV) are from Ce^{4+} $3d_{3/2}$, and the peaks labelled as v (882.3 eV) and v''' (898.2 eV) are from Ce^{4+} $3d_{5/2}$. The peaks attributed to the Ce^{3+} species were labelled as u' (904.6 eV) and v' (885.8 eV). The calculated concentrations of Ce^{3+} is about 70% [45], consistent with XANES analysis in Fig. 2d. The presence of Ce^{3+} implies the formation of oxygen vacancies [46], confirmed by EPR characterization. CeO_x-S/$ZnIn_2S_4$ showed an obvious isotropic paramagnetic signal with a *g* value of 2.001, assigned to the electrons trapped by the oxygen vacancies (Fig. 3b) [47]. After irradiating CeO_x-S/$ZnIn_2S_4$ hybrid catalyst at 440 nm, remarkable increase of the paramagnetic signal emerged. By contrast, pristine $ZnIn_2S_4$ exhibited weaker EPR signals without no obvious change after irradiation, demonstrating the electron enrichment character of the CeO_x-S/$ZnIn_2S_4$ hybrid catalyst with respect to light.

3.2. Photocatalytic CO_2 reduction

Upon acquiring the structure of the CeO_x-S/$ZnIn_2S_4$ hybrid catalyst, we are now performing CO_2 photoreduction experiments under 9 W LEDs irradiation centered at 455 nm (Fig. 4) to unveil its photocatalytic properties. Gas chromatography (GC) was employed to identify and quantify the gas products, in which CO was detected as the reduction product and no detectable CO_2 reduction products generated in liquid phase. As displayed in Fig. 4a, pristine ceria nanoparticles have no CO_2 photoreduction activity under this condition. The CeO_x-S/$ZnIn_2S_4$ exhibits a CO productivity of 1.8 mmol g^{-1} with a rate of 0.18 mmol g^{-1} h^{-1}, roughly twice of that for pristine $ZnIn_2S_4$, while H_2 formation has no obvious change. Using the CeO_x-S/$ZnIn_2S_4$ as photocatalyst, the apparent quantum yield (AQY) was measured to be 1.34% at 455 nm. Besides, CeO_x-S/$ZnIn_2S_4$ hybrid photocatalysts exhibited satisfactory performance in CO_2 reduction under other light irradiation and even a scale-up reaction system (Table S1). These results are comparable to the recent reports for CO_2 reduction by heterogeneous photocatalysts [8,39,48,49]. To exclude the possibility that CO comes from any adventitious organic matter, we conducted the experiment under the same conditions except for replacing CO_2 with Ar and no detectable CO was generated, verifying that CO was derived from CO_2 reduction. In contrast, pristine $ZnIn_2S_4$ shows much higher activity of H_2 production, indicating CeO_x-S/$ZnIn_2S_4$ hybrid catalysts are more benefited to CO_2 reduction to CO. Furthermore, when the reaction was conducted in the dark, no CO and H_2 was detected, verifying that CO_2 reduction was driven by visible light irradiation.

3.3. Investigation of the promotional role of CeO_x-S nanoclusters in CeO_x-S/$ZnIn_2S_4$ hybrid catalysts

In general, the key step in photocatalytic CO_2 reduction specifically involves the carrier separation and the subsequent transfer of photogenerated electrons into catalytically active sites. To uncover the underlying reasons for the enhancement of CeO_x-S/$ZnIn_2S_4$ hybrid catalyst in CO_2 photoreduction. We firstly studied the promotional role of CeO_x-S nanoclusters in carrier separation efficiency by Kelvin probe force microscopy (KPFM) and time-resolved photoluminescence (TRPL) characterizations (Fig. 5). Fig. 5a shows that the contact potential difference (CPD) value of CeO_x-S/$ZnIn_2S_4$ decreases by 150 mV (from 75 mV to -75 mV) compared with $ZnIn_2S_4$, predicting a driving force of 150 mV for charge separation from the built-in electric field at CeO_x-S and $ZnIn_2S_4$ interface. The actual charge separation was demonstrated by the surface photovoltage (SPV), which is the illumination-induced changes in CPD signals. CeO_x-S/$ZnIn_2S_4$ yields a SPV of 235 mV, higher than that of pristine $ZnIn_2S_4$ (164 mV), giving direct evidence for the enhanced charge separation. The results shown in Fig. 5b indicate that the decay kinetics induced by oxygen vacancy exhibits a much longer lifetime ($\sim$17 ns) with respect to the intrinsic band-edge emission ($\sim$10 ns). Both the KPFM and TRPL results convincingly demonstrate the promotional role of CeO_x-S in reducing the carriers recombination

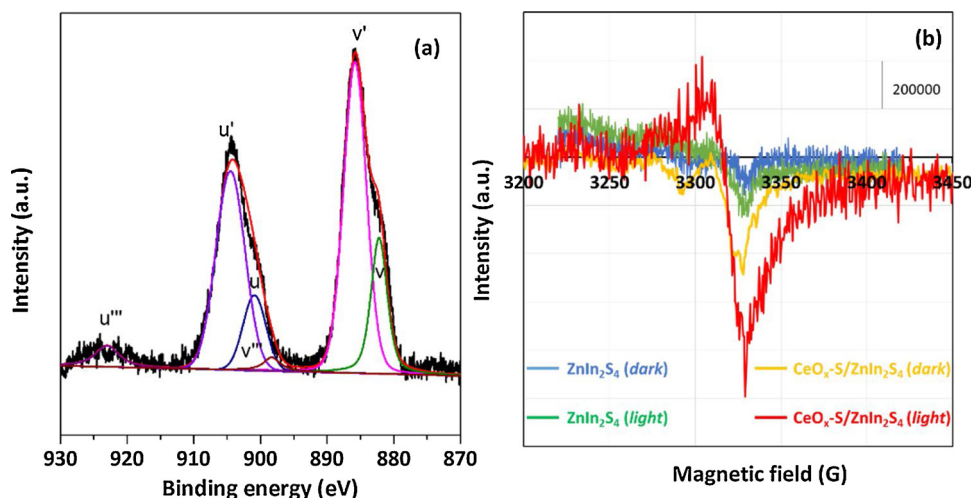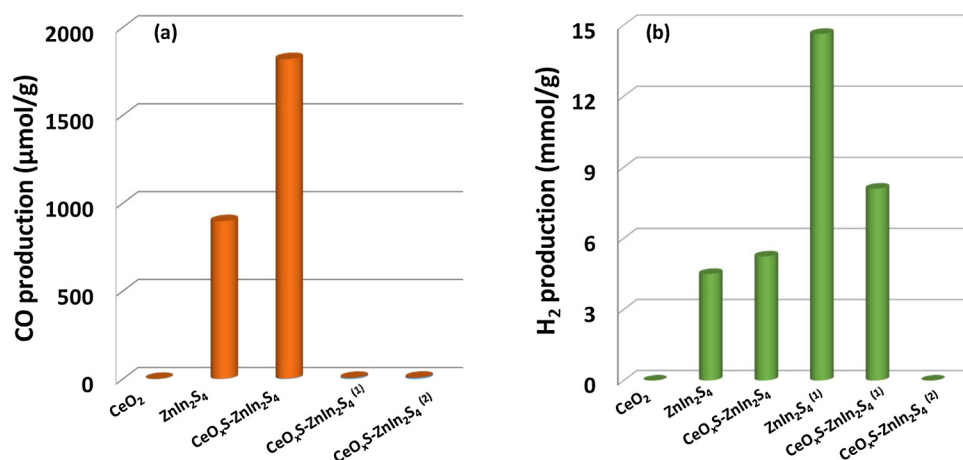**Fig. 3.** (a) XPS spectrum of Ce element in CeO_x-S/$ZnIn_2S_4$ hybrid catalyst and (b) characteristics of EPR signals on CeO_x-S/$ZnIn_2S_4$ and pristine $ZnIn_2S_4$.

Fig. 4. Comparison of different catalysts in photoreduction of CO_2 into CO under visible light irradiation. (a). CO production and (b). H_2 production. Standard reaction conditions: 10 mg of catalyst, 0.5 mL of H_2O, 0.5 mL of CH_3CN, 0.1 mL of triethylamine, 1 bar of CO_2, 9 W blue LEDs (455 nm), 42 °C, 10 h. [(1)] 1 bar of Ar was used instead. [(2)] In the dark (For interpretation of the references to colour in this figure legend, the reader is referred to the web version of this article).

[50].

To further reveal how CeO_x-S nanoclusters in CeO_x-S/ $ZnIn_2S_4$ hybrid catalyst influence the following transfer of electrons, we performed in situ EPR experiments (Fig. 6a), and the corresponding quantitative analysis by double integral of the EPR signals were displayed in Fig. 6b. In comparison with the dark conditions, the signal intensity (g = 2.001) remarkably increased by about 9 times when turning on the light, indicating the photogenerated electrons are captured by the oxygen vacancies [47]. Note that this signal intensity is almost unchanged when turning off the light, suggesting that CeO_x-S can serve as an electron tank under visible light irradiation. After injecting CO_2 to the system, the signal (g = 2.001) is almost restored to the initial state, implying that CO_2 can directly quench the trapped electrons. Thereby, the photogenerated electrons transfer to CO_2, benefiting the activation of CO_2. To further confirm the reliability of the results, the above experiments were further conducted for the sample treated by a light/quench cycle. We obtained similar variation of the EPR signal when turning on/off the light (Figure S8). Same as the first cycle, the signal intensity has little change when turning off the light while a sharp drop in signal intensity is observed after injecting CO_2 (Figure S8).

We then adopted in situ FTIR experiment to thoroughly understand the CO_2 adsorption and reaction intermediates over CeO_x-S/$ZnIn_2S_4$ (Fig. 6c) [10]. During the measurement, backgrounds are deducted from all spectra to exclude environmental factors. The catalyst was firstly exposed to a mixture of water vapor, CO_2 and Ar for 20 min in the dark before recording the IR spectra. The FTIR spectrum shows characteristic peaks owing to the vibrations of adsorbed CO_2. The bands

located at 1650, 1627 and 1445 cm^{-1} can be assigned to the bidentate bicarbonate (b−HCO_3−), while the peaks at 1592, 1349 and 1390 cm^{-1} can be assigned to the bidentate carbonate (b−CO_3^{2-}) and monodentate carbonate (m−CO_3^{2-}), respectively [51–54]. In comparison, the signal intensity of adsorbed CO_2 over pristine $ZnIn_2S_4$ is quite weak (Figure S9), indicating the weaker adsorption of CO_2 on pristine $ZnIn_2S_4$ relative to CeO_x-S/ $ZnIn_2S_4$. A much higher CO_2 onset desorption temperature for CeO_x-S/$ZnIn_2S_4$ (Figure S10) convictively demonstrates the promotional role of CeO_x-S nanoclusters in CO_2 adsorption. DFT calculations further illustrate the CO_2 optimally adsorbs on CeO_x-S nanoclusters with the adsorption energy of −1.67 eV, much stronger than on $ZnIn_2S_4$ (−0.18 eV) (Fig. 6d, e).

The IR cell was then continuously irradiated (200 mW·cm^{-2}, 440 nm) to acquire the information of reaction species and their intermediates. The characteristic absorption peaks at 1550, 1304 and 1260 cm^{-1} emerge, which can be attributed to COOH* and CO_2– groups. The intensity of the peaks gradually raised when the irradiation time prolonged to 60 min. The direct detection of these key species suggests that CO_2 was reduced to CO via the COOH* route [55–57]. With the same methods, we cannot observe the characteristic absorption peaks attributed to COOH* and CO_2– groups over pristine $ZnIn_2S_4$ (Figure S9), which further confirms the promotional role of CeO_x-S nanoclusters in CO_2 reduction. As for the selectivity in CO_2 photoreduction, CO is usually considered as the intermediate of CH_4 [58]. In this work, no detectable CH_4 is observed due to the weak adsorption of CO on CeO_x-S (-0.35 eV) and $ZnIn_2S_4$ (-0.13 eV), which leads to the CO direct desorption upon its formation (Fig. 6f, g).
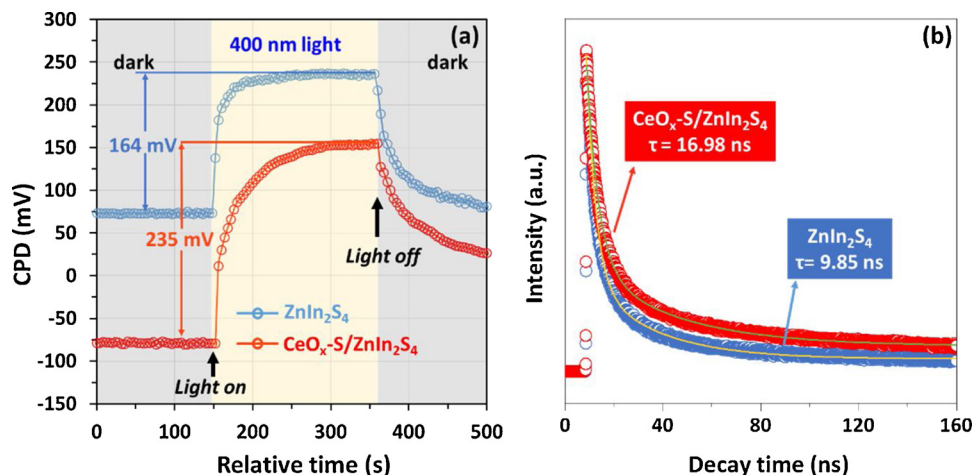
Fig. 5. Investigation of the promotional role of CeO_x-S nanoclusters in carrier separation efficiency. (a) CPD variation and (b) TRPL spectra of pristine $ZnIn_2S_4$ and CeO_x-S/$ZnIn_2S_4$.
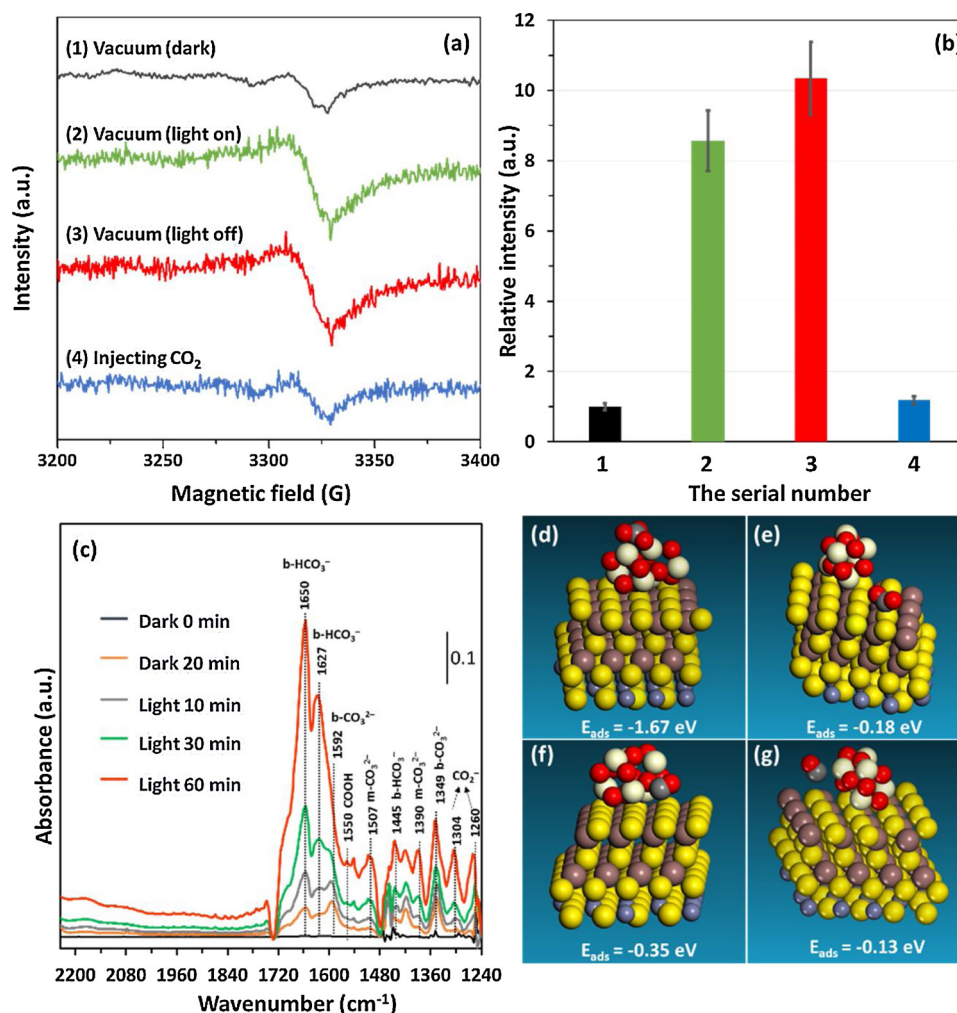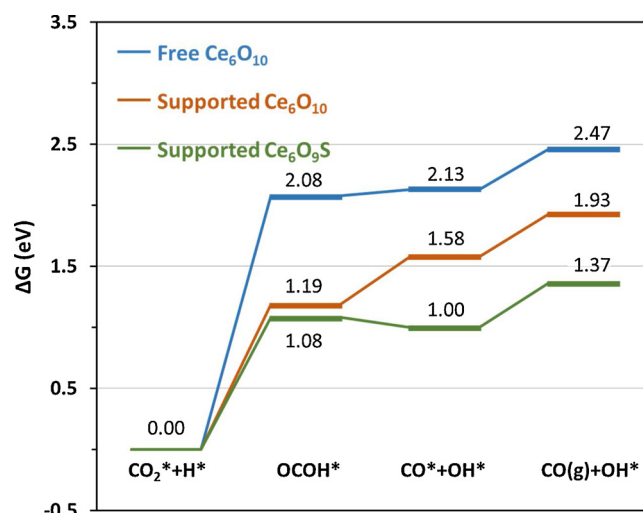
Fig. 6. Investigation of the promotional role of CeOₓ-S clusters in electron transfer and the subsequent surface reaction. (a) In situ EPR signals of CeOₓ-S/ZnIn₂S₄. (b) Quantitative analysis by double integral of the EPR signals in Fig. 6a. (c) In situ FTIR spectra for the adsorption, activation and reduction of CO₂ under visible light over CeOₓ-S/ZnIn₂S₄. (d, e) Adsorption energies of CO₂ and (f, g) CO at different sites of Ce₆O₁₀-ZnIn₂S₄ (0001) determined by DFT calculations.

3.4. Investigation of role of the coordination of cerium to sulfur by DFT calculations

To deeply gain insight into the role of the coordination of cerium to sulfur in CO_2 reduction, DFT calculations were further carried out on the reaction steps based on the in situ FTIR results. As indicated by the calculated reaction enthalpy change over different cerium oxide nanoclusters (Fig. 7 and Figure S11), the formation of COOH* is much more endergonic compared to that of CO*, indicating that the formation of COOH* intermediate is the rate-limited step. Notably, compared to the free Ce_6O_{10} clusters, the supported Ce_6O_{10} possesses the much lower formation energy of COOH*, which might attribute to the presence of a small amount of Ce–S at the interface. In spite of the presence of Ce–S obtained from EXAFS results, we still cannot confirm its exact location (interface or others). We then built another model (supported Ce_6O_9S), which also leads to much lower formation energy of COOH* compared to free Ce_6O_{10}, but similar to that of supported Ce_6O_{10}. This demonstrated that the presence of Ce–S in cerium oxide nanoclusters, regardless of its precise location, was in favor of the rate-limiting COOH* generation step, thus lowering the activation energy and explicitly facilitating the reduction of CO_2.

Fig. 7. Free energy diagrams of CO_2 reduction over free Ce_6O_{10}, supported Ce_6O_{10} (Ce_6O_{10}-ZnIn₂S₄ (0001)) and supported Ce_6O_9S (Ce_6O_9S-ZnIn₂S₄ (0001)).

4. Conclusions

In summary, we successfully prepared ultra-fine CeOₓ-S

nanoclusters highly dispersed on $ZnIn_2S_4$. In-depth investigations reveal that partial sulfurization are responsible for the rich Ce^{3+} and oxygen vacancies, which can increase CO_2 adsorption and electron-hole separation efficiency. On the strength of these advantages, CO_2 reduction is accelerated by two times over CeO_x-S/$ZnIn_2S_4$ under visible light. Further DFT calculations unveil the coordination of cerium to sulfur can lower activation energy barrier during CO_2 reduction by modulating surface electronic properties of catalysts, opening new avenues toward achieving robust visible light-driven CO_2 conversion performances. We believe this work is instructive to the design of active photocatalysts for achieving highly efficient solar chemical productions.

Acknowledgments

Appendix A. Supplementary data

Supplementary material related to this article can be found, in the online version, at doi:https://doi.org/10.1016/j.apcatb.2018.12.059.

References

[1] S. Liu, H. Tao, L. Zeng, Q. Liu, Z. Xu, Q. Liu, J.L. Luo, Shape-dependent electro-catalytic reduction of CO_2 to CO on triangular silver nanoplates, J. Am. Chem. Soc. 139 (2017) 2160–2163.

[2] J.L. White, M.F. Baruch, J.E. Pander Iii, Y. Hu, I.C. Fortmeyer, J.E. Park, T. Zhang, K. Liao, J. Gu, Y. Yan, T.W. Shaw, E. Abelev, A.B. Bocarsly, Light-driven heterogeneous reduction of carbon dioxide: photocatalysts and photoelectrodes, Chem. Rev. 115 (2015) 12888–12936.

[3] J. Jia, C. Qian, Y. Dong, Y.F. Li, H. Wang, M. Ghoussoub, K.T. Butler, A. Walsh, G.A. Ozin, Heterogeneous catalytic hydrogenation of CO_2 by metal oxides: defect engineering - perfecting imperfection, Chem. Soc. Rev. 46 (2017) 4631–4644.

[4] M. Zhou, S. Wang, P. Yang, C. Huang, X. Wang, Boron carbon nitride semiconductors decorated with CdS nanoparticles for photocatalytic reduction of CO_2, ACS Catal. 8 (2018) 4928–4936.

[5] S. Wang, X. Wang, Photocatalytic CO_2 reduction by CdS promoted with a zeolitic imidazolate framework, Appl. Catal. B 162 (2015) 494–500.

[6] S. Wang, B.Y. Guan, Y. Lu, X.W.D. Lou, Formation of hierarchical In_2S_3–$CdIn_2S_4$ heterostructured nanotubes for efficient and stable visible light CO_2 reduction, J. Am. Chem. Soc. 139 (2017) 17305–17308.

[7] G. Yang, D. Chen, H. Ding, J. Feng, J.Z. Zhang, Y. Zhu, S. Hamid, D.W. Bahnemann, Well-designed 3D $ZnIn_2S_4$ nanosheets/TiO_2 nanobelts as direct Z-scheme photocatalysts for CO_2 photoreduction into renewable hydrocarbon fuel with high efficiency, Appl. Catal. B 219 (2017) 611–618.

[8] S. Wang, B.Y. Guan, X.W.D. Lou, Construction of $ZnIn_2S_4$-In_2O_3 hierarchical tubular heterostructures for efficient CO_2 photoreduction, J. Am. Chem. Soc. 140 (2018) 5037–5040.

[9] E.V. Kondratenko, G. Mul, J. Baltrusaitis, G.O. Larrazábal, J. Pérez-Ramírez, Status and perspectives of CO_2 conversion into fuels and chemicals by catalytic, photocatalytic and electrocatalytic processes, Energy Environ. Sci. 6 (2013) 3112–3135.

[10] X. Chang, T. Wang, J. Gong, CO_2 photo-reduction: insights into catalysis and reaction on surfaces of photocatalysts, Energy Environ. Sci. 9 (2016) 2177–2196.

[11] C. Peng, G. Reid, H. Wang, P. Hu, Perspective: photocatalytic reduction of CO_2 to solar fuels over semiconductors, J. Chem. Phys. 147 (2017) 030901.

[12] M. Zhou, S. Wang, P. Yang, Z. Luo, R. Yuan, A.M. Asiri, M. Wakeel, X. Wang, Layered heterostructures of ultrathin polymeric carbon nitride and $ZnIn_2S_4$ nanosheets for photocatalytic CO_2 reduction, Chem. Eur. J. 24 (2018) 1–7.

[13] J. Graciani, K. Mudiyanselage, F. Xu, A.E. Baber, J. Evans, S.D. Senanayake, D.J. Stacchiola, P. Liu, J. Hrbek, J.F. Sanz, J.A. Rodriguez, Highly active copper-ceria and copper-ceria-titania catalysts for methanol synthesis from CO_2, Science 345 (2014) 546–550.

[14] F. Calaza, C. Stiehler, Y. Fujimori, M. Sterrer, S. Beeg, M. Ruiz-Oses, N. Nilius, M. Heyde, T. Parviainen, K. Honkala, H. Hakkinen, H.J. Freund, Carbon dioxide activation and reaction induced by electron transfer at an oxide-metal interface, Angew. Chem., Int. Ed 54 (2015) 12484–71248.

[15] X. Yang, S. Kattel, S.D. Senanayake, J.A. Boscoboinik, X. Nie, J. Graciani, J.A. Rodriguez, P. Liu, D.J. Stacchiola, J.G. Chen, Low pressure CO_2 hydrogenation to methanol over gold nanoparticles activated on a CeO_x/TiO_2 interface, J. Am. Chem. Soc. 137 (2015) 10104–10107.

[16] R. Long, Y. Li, Y. Liu, S. Chen, X. Zheng, C. Gao, C. He, N. Chen, Z. Qi, L. Song,

[17] J. Jiang, J. Zhu, Y. Xiong, Isolation of Cu atoms in Pd lattice: forming highly selective sites for photocatalytic conversion of CO_2 to CH_4, J. Am. Chem. Soc. 139 (2017) 4486–4492.

[17] A. Crake, K.C. Christoforidis, A. Kafizas, S. Zafeiratos, C. Petit, CO_2 capture and photocatalytic reduction using bifunctional TiO_2 /MOF nanocomposites under UV–vis Irradiation, Appl. Catal. B 210 (2017) 131–140.

[18] F. Esch, S. Fabris, L. Zhou, T. Montini, C. Africh, P. Fornasiero, G. Comelli, R. Rosei, Electron localization determines defect formation on Ceria substrates, Science 309 (2005) 752–755.

[19] Y. Ji, Y. Luo, New Mechanism for photocatalytic reduction of CO_2 on the anatase TiO_2(101) surface: the essential role of oxygen vacancy, J. Am. Chem. Soc. 138 (2016) 15896–15902.

[20] L. Wang, Y. Wang, Y. Cheng, Z. Liu, Q. Guo, M.N. Ha, Z. Zhao, Hydrogen-treated mesoporous WO_3 as a reducing agent of CO_2 to fuels (CH_4 and CH_3OH) with enhanced photothermal catalytic performance, J. Mol. Catal. A Chem. 4 (2016) 5314–5322.

[21] L. Liu, H. Zhao, J.M. Andino, Y. Li, Photocatalytic CO2 reduction with H2O on TiO2 nanocrystals: comparison of anatase, rutile, and brookite polymorphs and exploration of surface chemistry, ACS Catal. 2 (2012) 1817–1828.

[22] S. Sun, M. Watanabe, J. Wu, Q. An, T. Ishihara, Ultrathin $WO_3.0.33H_2O$ nanotubes for CO_2 photoreduction to acetate with high selectivity, J. Am. Chem. Soc. 140 (2018) 6474–6482.

[23] G. Xi, S. Ouyang, P. Li, J. Ye, Q. Ma, N. Su, H. Bai, C. Wang, Ultrathin $W_{18}O_{49}$ nanowires with diameters below 1 nm: synthesis, near-infrared absorption, photoluminescence, and photochemical reduction of carbon dioxide, Angew. Chem., Int. Ed 51 (2012) 2395–2399.

[24] C. Yang, Q. Li, Y. Xia, K. Lv, M. Li, Enhanced visible-light photocatalytic CO_2 reduction performance of $ZnIn_2S_4$ microspheres by using CeO_2 as cocatalyst, Appl. Surf. Sci. 464 (2018) 388–395.

[25] X. Gou, F. Cheng, Y. Shi, L. Zhang, S. Peng, J. Chen, P. Shen, Shape-controlled synthesis of ternary chalcogenide $ZnIn_2S_4$ and $CuIn(S,Se)_2$ nano-/microstructures via facile solution route, J. Am. Chem. Soc. 128 (2006) 7222–7229.

[26] L. Li, S. Kuwamoto, E. Fujimura, K. Yokoyama, Y. Urushihara, J. Matsui, A. Co, G.L. Leal, R.H. Colby, A.J. Giacomin, SAXS studies on agglomerative silica suspension under shear, AIP Conf. Proc. 1027 (2008) 779–781.

[27] B. Ravel, M. Newville, Artemis Athena, HEPHAESTUS: data analysis for X-Ray absorption spectroscopy using IFEFFIT, J. Synchrotron Radiat. 12 (2005) 537–541.

[28] M. Muñoz, P. Argoul, F. Farges, Continuous cauchy wavelet transform analyses of EXAFS spectra: a qualitative approach, Am. Mineral. (2003) 694–700.

[29] H. Li, Y. Gao, Y. Zhou, F. Fan, Q. Han, Q. Xu, X. Wang, M. Xiao, C. Li, Z. Zou, Construction and nanoscale detection of interfacial charge transfer of elegant Z-Scheme WO_3/Au/In_2S_3 nanowire arrays, Nano Lett. 16 (2016) 5547–5552.

[30] G. Kresse, J. Furthmuller, Efficient iterative schemes for ab initio total-energy calculations using a plane-wave basis set, Phys. Rev. B 54 (1996) 11169–11186.

[31] G. Kresse, J. Furthmuller, Efficiency of ab-initio total energy calculations for metals and semiconductors using a plane-wave basis set, Comput. Mater. Sci. 6 (1996) 15–50.

[32] J.P. Perdew, K. Burke, M. Ernzerhof, Generalized gradient approximation made simple, Phys. Rev. Lett. 77 (1996) 3865–3868.

[33] P.E. Blochl, Projector augmented-wave method, Phys. Rev. B 50 (1994) 17953–17979.

[34] G. Kresse, D. Joubert, From Ultrasoft pseudopotentials to the projector augmented-wave method, Phys. Rev. B 59 (1999) 1758–1775.

[35] S. Grimme, J. Antony, S. Ehrlich, H. Krieg, A consistent and accurate ab initio parametrization of density functional dispersion correction (DFT-D) for the 94 elements H-Pu, J. Chem. Phys. 132 (2010) 154104.

[36] F.G. Donika, G.A. Kiosse, S.I. Radautsan, S.A. Semiletov, I.G. Mustya, Crystal structure of the two pack polytypic form $ZnIn_2S_4$ (II)B, Kristallografiya 17 (1972) 663–665.

[37] Y. Lin, Z. Wu, J. Wen, K. Ding, X. Yang, K.R. Poeppelmeier, L.D. Marks, Adhesion and atomic structures of gold on Ceria nanostructures: the role of surface structure and oxidation state of Ceria Supports, Nano Lett. 15 (2015) 5375–5381.

[38] A.K.P. Mann, Z. Wu, F.C. Calaza, S.H. Overbury, Adsorption and reaction of acetaldehyde on shape-controlled CeO_2 nanocrystals: elucidation of structure–function relationships, ACS Catal. 4 (2014) 2437–2448.

[39] X. Jiao, Z. Chen, X. Li, Y. Sun, S. Gao, W. Yan, C. Wang, Q. Zhang, Y. Lin, Y. Luo, Y. Xie, Defect-mediated electron-hole separation in one-unit-cell $ZnIn_2S_4$ layers for boosted solar-driven CO_2 reduction, J. Am. Chem. Soc. 139 (2017) 7586–7594.

[40] J.A. Rodriguez, J.C. Hanson, D. Stacchiola, S.D. Senanayake, In situ/operando studies for the production of hydrogen through the water-gas shift on metal oxide catalysts, Phys. Chem. Chem. Phys. 15 (2013) 12004–12025.

[41] S. Wada, K. Oka, K. Watanabe, Y. Izumi, Catalytic conversion of carbon dioxide into dimethyl carbonate using reduced copper-cerium oxide catalysts as Low as 353 K and 1.3 MPa and the reaction mechanism, Front. Chem. 1 (2013) 8.

[42] A.E.Pd. Lima, D.Cd. Oliveira, In situ XANES study of cobalt in Co-Ce-Al catalyst applied to steam reforming of ethanol reaction, Catal. Today 283 (2017) 104–109.

[43] T. Baidya, P. Bera, O. Krocher, O. Safonova, P.M. Abdala, B. Gerke, R. Pottgen, K.R. Priolkar, T.K. Mandal, Understanding the anomalous behavior of Vegard's Law in $Ce_{1-x}M_xO_2$ (M = Sn and Ti; 0 < x < /= 0.5) solid solutions, Phys. Chem. Chem. Phys. 18 (2016) 13974–13983.

[44] C. Li, X. Liu, G. Lu, Y. Wang, Redox properties and CO_2 capture ability of CeO_2 prepared by a glycol solvothermal method, Chin. J. Catal. 35 (2014) 1364–1375.

[45] H. Zhao, Y. Dong, P. Jiang, G. Wang, J. Zhang, Highly dispersed CeO_2 on TiO_2 nanotube: a synergistic nanocomposite with superior peroxidase-like activity, ACS Appl. Mater. Interfaces 7 (2015) 6451–6461.

[46] Matteo. Cargnello, Vicky V.T. Doan-Nguyen, Thomas R. Gordon, Rosa E. Diaz, Eric

A. Stach, Raymond J. Gorte, Paolo Fornasiero, C.B. Murray, Control of metal na-nocrystal size reveals metal-support interface role for Ceria catalysts, Science 341 (2013) 771–773.

[47] B. Chen, X. Li, R. Zheng, R. Chen, X. Sun, Bimetallic (Au–Cu core)@(ceria shell) nanotubes for photocatalytic oxidation of benzyl alcohol: improved reactivity by Cu, J. Mol. Catal. A Chem. 5 (2017) 13382–13391.

[48] Y. Zhu, Z. Xu, Q. Lang, W. Jiang, Q. Yin, S. Zhong, S. Bai, Grain boundary en-gineered metal nanowire cocatalysts for enhanced photocatalytic reduction of carbon dioxide, Appl. Catal. B 206 (2017) 282–292.

[49] S. Wang, B.Y. Guan, Y. Lu, X.W.D. Lou, Formation of hierarchical In_2S_3-$CdIn_2S_4$ heterostructured nanotubes for efficient and stable visible light CO_2 reduction, J. Am. Chem. Soc. 139 (2017) 17305–17308.

[50] T. Montini, M. Melchionna, M. Monai, P. Fornasiero, Fundamentals and catalytic applications of CeO_2-Based materials, Chem. Rev. 116 (2016) 5987–6041.

[51] K. Pokrovski, K.T. Jung, A.T. Bell, Investigation of CO and CO_2 adsorption on tet-ragonal and monoclinic zirconia, Langmuir 17 (2001) 4297–4303.

[52] Y. Wang, J. Zhao, T. Wang, Y. Li, X. Li, J. Yin, C. Wang, CO_2 photoreduction with H_2O vapor on highly dispersed CeO_2/TiO_2 catalysts: surface species and their

reactivity, J. Catal. 337 (2016) 293–302.

[53] D.C. Sorescu, S. Civiš, K.D. Jordan, Mechanism of oxygen exchange between CO_2 and TiO_2(101) anatase, J. Phys. Chem. C 118 (2014) 1628–1639.

[54] W.J. Yin, M. Krack, B. Wen, S.Y. Ma, L.M. Liu, CO_2 capture and conversion on rutile TiO_2(110) in the water environment: insight by first-principles calculations, J. Phys. Chem. Lett. 6 (2015) 2538–2545.

[55] L.C. Grabow, M. Mavrikakis, Mechanism of methanol synthesis on Cu through CO_2 and CO hydrogenation, ACS Catal. 1 (2011) 365–384.

[56] P. Taheri, T. Hauffman, J.M.C. Mol, J.R. Flores, F. Hannour, J.H.W. de Wit, H. Terryn, Electrochemical analysis of the adsorption and desorption behaviors of carboxylic acid and anhydride monomers onto zinc surfaces, Electrochim. Acta 56 (2011) 9317–9323.

[57] W. Zhang, X. Li, Q. Zhao, Y. Hou, Y. Shen, G. Chen, Uniform α-Fe_2O_3 nanotubes fabricated for adsorption and photocatalytic oxidation of naphthalene, Mater. Chem. Phys. 129 (2011) 683–687.

[58] S. Neatu, J.A. Macia-Agullo, P. Concepcion, H. Garcia, Gold-copper nanoalloys supported on TiO_2 as photocatalysts for CO_2 reduction by water, J. Am. Chem. Soc. 136 (2014) 15969–15976.